Accepted Manuscript

A predictive tool for determining patient-specific mechanical properties of human corneal tissue

Miguel Ángel Ariza-Gracia, Santiago Redondo, David Piñero Llorens, Begoña Calvo, José Felix Rodriguez Matas

Please cite this article as: M.. Ariza-Gracia, S. Redondo, D.P. Llorens, B. Calvo, J.F. Rodriguez Matas, A predictive tool for determining patient-specific mechanical properties of human corneal tissue, *Comput. Methods Appl. Mech. Engrg.* (2016), http://dx.doi.org/10.1016/j.cma.2016.12.013

A Predictive Tool for Determining Patient-Specific Mechanical Properties of Human Corneal Tissue

Miguel Ángel Ariza–Gracia[a,b], Santiago Redondo[a], David Piñero Llorens[c,d], Begoña Calvo[a,f], José Felix Rodriguez Matas[e]

[a]*Department of Mechanical Engineering, Aragón Institute of Engineering Research –i3A–, Zaragoza, Spain*
[b]*Institute for Surgical Technology and Biomechanics, University of Bern, Switzerland*
[c]*Ophthalmology Department –OFTALMAR–, Medimar International Hospital, Alicante, Spain*
[d]*Optics, Pharmacologist and Anatomy Department, University of Alicante, Alicante, Spain*
[e]*LaBS, Department of Chemistry, Materials and Chemical Engineering "Giulio Natta", Politecnico di Milano, Milano, Italy*
[f]*CIBER de Bioingeniería, Biomateriales y Nanomedicina (CIBER-BBN), Aragon Health Sciences Institute, Spain*

Abstract

A computational predictive tool for assessing patient-specific corneal tissue properties is developed. This predictive tool considers as input variables the corneal central thickness (CCT), the intraocular pressure (IOP), and the maximum deformation amplitude of the corneal apex (U) when subjected to a non-contact tonometry test. The proposed methodology consists of two main steps. First, an extensive dataset is generated using Monte Carlo (MC) simulations based on finite element models with patient-specific geometric features that simulate the non-contact tonometry test. The cornea is assumed to be an anisotropic tissue to reproduce the experimentally observed mechanical behavior. A clinical database of 130 patients (53 healthy, 63 keratoconic and 14 post-LASIK surgery) is used to generate a dataset of more than 9,000 cases by permuting the material properties. The second step consists of constructing predictive models for the material parameters of the constitutive model as a function of the input variables. Four different approximations are explored: quadratic response surface (QRS) approximation, multiple layer perceptron (MLP), support vector regressor (SVR), and K-nn search. The models are validated against data from five real patients. The material properties obtained with the predicted models lead to a simulated corneal displacement that is within 10% error of the measured value in the worst case scenario of a patient with very advanced keratoconus disease. These results demonstrate the potential and soundness of the proposed methodology.

1

1. Introduction

Corneal biomechanics is an open topic in ophthalmology. Precise knowledge about the underlying factors that affect the corneal mechanical response will allow establishing better clinical diagnoses, monitoring the progression of different diseases (e.g., keratoconus, a non-inflammatory disease that causes disruption of the collagen fibers) or designing a priori patient-specific surgical plans that may reduce the occurrence of unexpected outcomes.

Non-contact tonometry has recently gained interest as a diagnostic tool in ophthalmology and as an alternative method for characterizing the mechanical behavior of the cornea. In a non-contact tonometry test, a high-velocity air jet is applied to the cornea for a very short time (less than 30 ms), causing the cornea to deform, while the corneal motion is recorded by a high-speed camera. A number of biomarkers associated with the motion of the cornea, i.e., maximum corneal displacement and time between first and second applanations, among others, have been proposed to characterize pre- and post-operative biomechanical changes[1, 2, 3, 4, 5, 6, 7, 8, 9]. However, this response is the result of the interplay between the geometry of the cornea, the intraocular pressure (IOP), and the mechanical behavior of the corneal tissue, as has been demonstrated by recent experimental and numerical studies [2, 10]. These studies suggest that this interplay could be the reason for some unexpected clinical results (i.e., a softer cornea with a higher IOP could show the same behavior as a stiffer cornea with a lower IOP). Although the geometry and the IOP can be measured using corneal topographers and Goldmann tonometry applanation tests (GATs), the mechanical behavior of the cornea cannot be directly characterized *in vivo*.

The human cornea is composed of an almost incompressible layered base material (matrix), mainly composed of water, where two families of orthogonal collagen fibers are embedded [11,

12]. Due to this structure, the tissue behaves as an anisotropic solid that has two preferential directions corresponding to the direction of the collagen fibers. A number of material models have been proposed to reproduce the behavior of the cornea, ranging from simply hyperelastic isotropic materials [13] to more complex models coupling the hyperelastic isotropic response for the matrix (neo-Hookean models) with the anisotropic response of the collagen fibers of the eye [12, 14, 15, 16, 17, 18, 23, 24]. These material models have been incorporated into computer models of the eye to simulate surgical interventions and tonometry tests in an effort to demonstrate the potential of these *in silico* models[3, 4, 17, 25, 26, 27, 28, 54, 55, 56].

However, numerical studies have found that the contribution of the fibers to load bearing during a tonometry test is highly reduced due to the bending mode of deformation imposed by the test. Under this particular loading condition, other factors such as the IOP or the central corneal thickness (CCT) were found to be more significant in the response of the cornea to the air puff[2, 4]. Moreover, in the physiological range of IOP (from 10 to 15 mmHg) and CCT (from 500 to 600 microns), the corneal tissue is not subjected to large stresses, with the fibers bearing relatively low loads[4]. In addition, experimental studies in porcine and human eyes have demonstrated that fibers play a major role only when the IOP increases to values above the physiological range [24, 29]. Therefore, it appears that the mechanical behavior of the matrix will play a significant role in reproducing the corneal response during a tonometry test. Furthermore, some authors have suggested that only one in vivo technique may not be sufficiently accurate for properly characterizing the material properties, such as Kok et al. [19, 4]. However, at present, it is the only clinical device that permits a non-invasive analysis of the human cornea, as biaxial or inflation tests can only be performed ex vivo.

Over the past decade, with the development of large and extensive datasets, the use of artificial neural networks (ANNs) has returned to the spotlight. Essentially, an ANN intends to model the human brain by mathematically reproducing the neural architecture to learn and recognize patterns or to adjust functional responses. In ophthalmology, commercial topographers implement different types of ANNs to establish a classification between healthy eyes and diseased eyes (e.g., keratoconus eyes, KTC, or ectasias post-LASIK)[30, 31, 32, 33, 34]. Unfortunately,

3

these ANNs are primarily based on the geometrical features of the cornea (e.g., radii, thickness, diopters, shape factors, and so forth), and it is not common to consider mechanical variables such as the intraocular pressure (IOP). In addition to ANNs, response surface methods have also been used in biomedical sciences for predicting the effects of different model parameters on a set of biomarkers associated with a particular pathology [35, 36, 37]. The great interest in these mathematical methods relies on the immediateness of their response, which is a key factor for clinical applications. However, they suffer from an important weakness: the extension of the training dataset. These methods are based on precisely learning a considerable amount of data under different conditions to lead to a proper and accurate response of the system. Otherwise, a poor prediction or an overfitting in the solution could be reached with catastrophic results. Unfortunately, the higher the complexity of the applied neural network, the higher the number of cases that are needed for both training and validating the training. Therefore, this is a clear limiting factor when dealing with patient data. Apart from the aforementioned mathematical tools, another optimization approach has been used for determining the material properties of the human cornea: the inverse finite element method (henceforth IFEM) [3, 20, 21, 22]. This method uses an iterative optimization procedure that changes a set of unknown parameters to match the numerical response with the experimental response. Thus, it requires a highly accurate definition of the problem and sufficiently reliable boundary conditions. Moreover, each case of interest must be evaluated ad hoc, resulting in a time-consuming process that is not real time and hence not interesting for real clinical applications.

The present work aims to construct predictors for real-time clinical applications based on ANN and quadratic response surface (QRS) approximations to obtain the parameters of the constitutive model of a patient's cornea using 3 clinical biomarkers as inputs: the maximum corneal displacement measured during a non-contact tonometry test (U), the patient's IOP, and geometrical features of the cornea. The predictive tool relies on a dataset generated by the results of finite element simulations of the non-contact tonometry test. The simulations are based on combinations of patients of a real clinical database (the patient-specific corneal geometry and the Goldmann IOP[4]) and of corneal material properties of the numerical model to predict the corneal apical

4

displacement. In brief, the finite element model is used to perform a Monte Carlo (MC) simulation in which the material parameters and the IOP are uniformly varied within an established range. The range for the material parameters was determined by considering the experimental results from an inflation test reported in the literature[24, 38] and the physiological response of the cornea to an air-puff device (i.e., displacement of the cornea using a CorVis device). First, the inflation tests were used to initially screen the model parameters, to constrain the search space of the optimization and in an attempt to avoid an ill-posed solution [19]. Second, the range of each material parameter was then determined such that the *in silico* inflation curve was within the experimental window. In this way, both physiological behaviors of the cornea are simultaneously fulfilled: the response to an inflation test (biaxial stress) and the response to an air-puff test (bending stress). Subsequently, the generated dataset was used to implement different predictors for the mechanical properties of the patient's corneal model in terms of variables that are identified in a standard non-contact tonometry test. Eventually, the resulting models were tested on five different, new and unknown patients to demonstrate the potential and soundness of the proposed methodology in terms of predicting corneal tissue properties.

2. Materials and Methods

2.1. Patient data

Topographical data of the cornea and IOP from 130 patients (53 healthy, 63 keratoconic and 14 post-LASIK surgery)[2, 4] were collected prospectively, i.e., an ongoing measuring process without posterior revision of the patient's medical history, at the Department of Ophthalmology (OFTALMAR) of the Vithas Medimar International Hospital (Alicante, Spain). A comprehensive ophthalmologic examination was performed in all cases, including Goldmann tonometry and analysis of the corneal anterior and posterior segments using a Scheimpflug photography-based topography system (Pentacam system, Oculus, Germany). The inclusion criteria were as follows: healthy eyes, eyes diagnosed with keratoconus according to the Rabinowitz criteria [39], and eyes that had undergone previous laser in situ keratomileusis (post-LASIK) for the correction of myopia (range -0.50 to -8.00 D). The exclusion criteria were patients with active ocular diseases

5

107 or patients with other types of previous ocular surgeries. Clinical validation data were collected

108 prospectively at the Qvision Ophthalmic Unit of the Vithas Virgen del Mar Hospital (Almeria,

109 Spain). A comprehensive ophthalmologic examination was performed in all cases, including

110 Goldmann tonometry, corneal and anterior segment analysis using a Scheimpflug photography-

111 based topography system (Pentacam, Oculus, Germany) and corneal dynamics analysis (CorVis,

112 Oculus, Germany). This study adhered to the guidelines of the Declaration of Helsinki and was

113 approved by the ethics committee of the University of Alicante (Alicante, Spain).

Figure 1: **Graphical Outline of the Developed Methodology.**

2.2. Construction of the predictive model

115 Figure 1 shows the main steps of the proposed methodology. As stated in the introduction, the

116 methodology relies on the use of a previously developed algorithm for the patient-specific geo-

117 metrical reconstruction of the cornea and the simulation of a non-contact tonometry test [4]. To

118 generate the dataset, two main steps have to be differentiated. In the first step, an initial screening

119 over the constitutive model parameters is performed using the inflation experiments reported in

120 the literature [24, 38]. There are two benefits associated with this step: constraining the space of

121 solutions for the subsequent step and restraining the space of solutions to those that behave phys-

122 iologically on the inflation range. The second step corresponds to the generation of the training

123 dataset using a Monte Carlo analysis. The *in silico* simulations of the non-contact tonometry

124 test using the clinical patient-specific corneal topography and the clinical Goldmann IOP are

125 used to obtain the bending behavior of the cornea. By filtering with the clinical ranges of max-

126 imum deformation amplitude [1], the space of material parameters that behave physiologically

127 in both experiments (inflation and air puff) is obtained. Following the Monte Carlo simulation,

128 an analysis of variance (ANOVA, using a second-order linear model for the sum of squares and

129 accounting for the interaction between the parameters) is performed to identify the impact of the

130 variables on the maximum displacement of the corneal apex, thereby defining the main inputs of

131 the predictors. The resulting dataset is then used to train a set of 4 different predictors in terms

132 of the material model parameters (D_1, D_2, k_1, and k_2) and the main variables identified through

6

ANOVA. Finally, the predictors are tested with clinical results from a non-contact tonometry test on five patients to validate the methodology using unknown patient data.

2.3. Finite Element Model

The FE model consists of the patient-specific corneal geometric data, which are provided by the topographer, the limbus and half of the sclera [4]. The geometry is meshed using quadratic hexahedral elements (62,276 nodes and 13,425 elements). The limbus and the cornea are considered to be anisotropic solids described by the same strain energy function but with different preferential directions (the cornea is assumed to be orthotropic with two orthogonal families of fibers, whereas the limbus is assumed to be transversely isotropic with only one family of fibers). The limbus is assumed to have the same material properties as the cornea since a proper in vivo characterization has not yet been reported and because it is considered to be a more compliant boundary condition for the cornea [56] far from the zone of influence of the air jet. Material models are described in detail in the following section. Conversely, the sclera is assumed to be an isotropic solid since the region of interest is far from the optic nerve insertion. Symmetry boundary conditions are defined on the scleral symmetry plane, and the intraocular pressure is assumed to be an equally distributed internal pressure determined by the Goldmann tonometry test.

To properly simulate the profile of pressure over the cornea of the non-contact tonometry from a purely structural perspective, a computational fluid dynamics simulation using ANSYS was conducted to determine the pressure pattern over the cornea due to the air puff. Although it is an approximation since the cornea is considered to be a rigid wall interface for the sake of the fluid analysis, a bell-shaped profile with a peak pressure set to 15 kPa is obtained (commercial devices range between 10 and 15 kPa), following a 30 ms temporal load profile provided by Oculus (only the load phase is considered). In addition, a zero-pressure algorithm is performed as a step prior to the air-puff simulation and is necessary for determining the corneal tissue pre-stress due to the IOP. Briefly, a fixed-point iterative optimization is applied, where an initial model of the eyeball is subjected to an internal pressure to deform. Subsequently, the error between the measured configuration (i.e., topographer geometry) and the deformed configuration is computed. If the

7

161 error is greater than a tolerance, a new initial model is computed by subtracting the point-to-point

162 error. Eventually, the algorithm stops once the measured reference is achieved when pressurizing

163 the initial (usually smaller) model (for further details, see [4]).

164 *2.4. Material Model*

165 The form of the strain energy function for modeling the cornea corresponds to a modified

166 version of that proposed by Gasser–Holzapfel–Ogden [40] for arterial tissue, where the neo-

167 Hookean term has been substituted by an exponential term

$$\psi(C, n_\alpha) = D_1 \cdot \{\exp[D_2 \cdot (\bar{I}_1 - 3)] - 1\} + \frac{k_1}{2 \cdot k_2} \cdot \sum_{\alpha=1}^{N} \{\exp[k_2\langle\bar{E}_\alpha\rangle^2] - 1\} + K_0 \cdot \left(\frac{J_{el}^2 - 1}{2} - \ln(J_{el})\right),$$

$$\text{with} \quad \bar{E}_\alpha \stackrel{\text{def}}{=} \kappa \cdot (\bar{I}_1 - 3) + (1 - 3\kappa) \cdot (\bar{I}_{4(\alpha\alpha)} - 1),$$

(1)

168 where C is the right Cauchy–Green tensor; $J_{el} = \sqrt{\det C}$ is the elastic volume ratio; D_1, D_2, k_1

169 and k_2 are material parameters; K_0 is the bulk modulus; N is the number of families of fibers; $\bar{I}_1$ is

170 the first invariant of the modified right Cauchy–Green Tensor $\bar{C} = J_{el}^{-2/3}C$; and $\bar{I}_{4(\alpha\alpha)} = n_\alpha \cdot \bar{C} \cdot n_\alpha$

171 is the square of the stretch along the fiber's direction n_α. The parameter κ describes the level of

172 dispersion in the fiber's direction and has been assumed to be zero since it has been reported that

173 a dispersion in the fibers of ± 10 deg about the main direction results in a maximum variation of

174 0.03% on the maximum corneal displacement [4].

175 The strain-like term $\bar{E}_\alpha$ in Eq. 1 characterizes the deformation of the family of fibers with

176 preferred direction n_α. The model assumes that collagen fibers bear load only in tension while

177 they buckle under compressive loading. Hence, only when the strain of the fibers is positive,

178 i.e., $\bar{E}_\alpha > 0$, do the fibers contribute in the strain energy function. This condition is enforced

179 by the term $< \bar{E}_\alpha >$, where the operator $< \cdot >$ stands for the Macauley bracket defined as

180 $< x > = \frac{1}{2}(|x| + x)$. The model has been implemented in a *UANISOHYPER* user subroutine within

181 the FE software *Abaqus*.

182 Due to the random distribution of fibers far from the optic nerve insertion, the sclera has been

8

assumed to be an isotropic hyperelastic material [41] (Eq. 2).

$$\psi_Y = \sum_{i=1}^{3} K_i (J_{el} - 1)^{2 \cdot i} + \sum_{i=1}^{3} C_{i0} \cdot (\bar{I}_1 - 3)^i, \tag{2}$$

where $C_{10} = 810$ [kPa], $C_{20} = 56,050$ [kPa], $C_{30} = 2,332,260$ [kPa], and K_i [kPa] is automatically set by the finite element solver during execution.

2.5. Monte Carlo Simulation

Due to the large dispersion in the corneal responses to inflation and air-puff tests and because the behavior of the fibers should not be properly characterized by a single experiment, the Monte Carlo simulation was conducted in two steps. First, the inflation experiments were used for screening the range of values of the material model that behaves physiologically in a biaxial stress state and hence constraining the searching space in subsequent steps. A total of 81 combinations of the material parameters were used to simulate an inflation test on an average healthy eye (see Figure 2b). The *in silico* inflation curves were then compared with experiments reported in the literature [24, 38], and the range of material parameters leading to curves within the experimental window was determined. The identified range of parameters was set to $D_1[kPa] \in (0.0492, 0.492)$, $D_2[-] \in (70, 144)$, $k_1[kPa] \in (15, 130)$, and $k_2[-] \in (10, 1000)$.

The second step was to generate the dataset using the Monte Carlo simulation and considering a uniformly distributed sample of the material parameters within the previously identified range. A uniform distribution was assumed since there are no a priori data on the dispersion of the mechanical parameters in the human cornea, and therefore, total ignorance about the population is assumed. Otherwise, a bias could be introduced on the outcome of the system. Additionally, to account for the physiological diurnal variations in the IOP [42], variations in the IOP ranging from 8 to 30 mmHg along with the patient's IOP at the moment of the examination were also considered in the Monte Carlo simulation. Hence, for each available geometry in the clinical database, 72 different samples of the material parameters and the IOP, uniformly distributed in their respective ranges, were used to conduct 72 simulations of the non-contact tonometry test. Consequently, a total of 9,360 computations (i.e., 72 combinations times 130 geometries) were

9

²⁰⁸ scheduled. The generated dataset consisted of the following variables: classification (healthy,

²⁰⁹ KTC and LASIK), computation exit status (failed or successful), material parameters (D_1, D_2,

²¹⁰ k_1 and k_2), IOP, CCT, nasal-temporal curvature (R_h), superior-inferior curvature (R_v) and the

²¹¹ computed maximum displacement of the cornea (U_{num}).

²¹² After the dataset was generated, ANOVA was performed to identify the most influential model

²¹³ parameters (geometry, pressure and material) on the numerical displacement, U_{num}, obtained

²¹⁴ with the non-contact tonometry simulation. The results from this analysis were used to identify

²¹⁵ the geometric parameters to be included in the construction of the predictor functions for the ma-

²¹⁶ terial parameters. ANOVA was conducted on the global dataset without differentiation between

²¹⁷ the populations and for each of the populations (healthy, keratoconus or KTC, and LASIK). Since

²¹⁸ the dataset is randomly generated, ANOVA cannot be directly conducted on the data. Instead, a

²¹⁹ quadratic response surface was first fit to U_{num} (e.g., $U_{num} = f(geometry, pressure, material)$).

²²⁰ Then, a Pareto analysis (i.e., it states the most influential parameters on an objective variable, ar-

²²¹ ranging them in decreasing order by taking into account the cumulative sum of the influence until

²²² reaching a 95% variation on the objective variable) was used to determine the most influential

²²³ parameters on the dependent variable, U_{num}.

2.6. Predictive Models

²²⁵ The generated dataset was used to construct predictors for the mechanical properties of the

²²⁶ patient's cornea in terms of variables that are measured with a standard non-contact tonometry

²²⁷ test. Two different approaches were implemented (see Fig.1): i) response surface approach and

²²⁸ ii) neighborhood-based approach.

2.6.1. Response surface approach

²³⁰ This approach is based on adjusting, or training, a predictor model for each material parameter

²³¹ (D_1, D_2, k_1 and k_2). Individual predictors were constructed using either an ANN or a quadratic

²³² response surface. For the ANN approach, two different mathematical models were considered:

²³³ multiple layer perceptron, MLP, and support vector regressor, SVR. As an alternative to the

²³⁴ ANN, a quadratic RS (QRS) was fit for each material parameter.

10

Artificial Neural Network: Multiple Layer Perceptron (MLP). An MLP is a feedforward ANN whose aim is to map a set of input variables (i.e., parameters that define the problem) into an output, allowing non-linear separable sets to be distinguished. It consists of different layers formed by 'neurons' or processing elements with non-linear activation: input layer, hidden layer and output layer. This technique is a supervised back-propagation learning technique for the training [57]. For the present study, an ensemble of 7 independent MLPs has been configured, obtaining the output as the average of the individual outputs (reducing the inherent variability of the method). Each independent MLP has been trained using a Levenberg-Marquardt minimization with early stooping criteria (usual criteria: a maximum of 6 increments of the validation error and a maximum of 1000 training epochs). Each MLP has 10 neurons for the hidden layer.

Support Vector Regressor (SVR). A support vector machine (SVM) is a supervised learning model that is mainly used for analyzing data for classification and regression analysis [58]. Once a set of training data is given, it marks each point for classifying into categories using a non-probabilistic non-linear classifier based on the use of kernels, which allow mapping into higher-dimensional feature spaces to better discern the clustering of categories. When the SVM is used for fitting a response (i.e., regression) rather than classifying, it is called a support vector regressor (SVR)[59]. For the present study, the libSVM C++ library using the epsilon-SVR formulation with a Gaussian kernel (RBF) was used for solving the SVR problem [43]. There are three configuration parameters: the *epsilon value* (default value 0.001), the algorithm *Cost* (optimized value) and the kernel's *Gamma* (optimized value). The optimization of the parameters was achieved by searching the *cross-validation generalized performance* of the training data. This method uses a grid search within the maximum expectation range of the parameters (*Cost* and *Gamma*), yielding a surface where the minimum corresponds to the optimum.

Regarding the dataset used for both methods (MLP and SVR), it has been split as 80% of the data for the training stage and 20% for the validation stage. In addition, the models have been trained using k-fold techniques (with a k-fold equal to 5) to automatically

11

²⁶³ optimize their parameters while avoiding overfitting during the training and differencing

²⁶⁴ datasets according to populations (healthy, KTC and LASIK). Furthermore, the data have

²⁶⁵ been normalized using the criterion of null average and the standard deviation equal to one.

²⁶⁶ **Quadratic Response Surface (QRS)**. The response surface methodology seeks for the

²⁶⁷ relationship between the input variables and the response variables in terms of the optimal

²⁶⁸ response and using a dataset constructed following a sequence of designed experiments

²⁶⁹ [60]. In general, the method fits a multiple order surface (e.g., a second-order polynomial)

²⁷⁰ to minimize the error with respect to the experimental data. In the present study, a multiple

²⁷¹ linear regression model including crossed and second-order terms was used for predicting

²⁷² the response (D_1, D_2, k_1 and k_2) as a linear function of the predictor variables. The model

²⁷³ fitting used a stepwise regression (i.e., terms can be added or removed depending on their

²⁷⁴ influence on the response) based on the Akaike information criterion (AIC) [44]. The AIC

²⁷⁵ provides a measure of model quality by simulating the situation where the model is tested

²⁷⁶ on a different data set. After computing several different models, they can be compared

²⁷⁷ using this criterion. According to Akaike's theory, the most accurate model has the smallest

²⁷⁸ AIC.

²⁷⁹ Independent predictors were fit to the entire dataset and to individual populations to test their

²⁸⁰ classification capabilities. Each predictor was structured as follows. Let j stand for a particular

²⁸¹ material parameter and χ_j be its predictor. Based on the ANOVA performed on the dataset, the

²⁸² most influential geometric parameters on the corneal displacement, U, are identified and denoted

²⁸³ as x. Hence, each predictor χ_j was constructed as a function (inputs) of x, IOP, and the remaining

²⁸⁴ material parameters of the model. Therefore, for parameter D_1, $\chi_{D_1} = \chi_{D_1}(x, IOP, D_2, k_1, k_2)$.

²⁸⁵ Once the models were trained, identification of the material parameters from the known patient

²⁸⁶ data, i.e., x, IOP, and U, was performed iteratively using a fixed-point iteration algorithm. The

²⁸⁷ search algorithm is detailed in Algorithm 1. In brief, D_1 is evaluated through χ_{D_1} using the

²⁸⁸ material parameters from the previous iteration; D_2 will then be obtained through χ_{D_2} including

²⁸⁹ the previously computed value for D_1, while k_1 and k_2 are kept from the previous iteration, and so

²⁹⁰ on. The cost function controls the changes in the values of the material parameters between two

12

consecutive iterations: if the change in the material properties between two consecutive iterations

is less than a tolerance, the algorithm stops and the identified material parameters are reported.

Algorithm 1. *Fixed-point iteration algorithm to determine material parameters from patient's*
data (clinical biomarkers).


```
%Initialize Control Values
TOL=1e-6; itemax=5000; k=1; error=1;
%Initialize Random Material Seed
```
$mat^k = (D_1^k \ D_2^k \ k_1^k \ k_2^k);$
WHILE *AND(error>TOL,k<itemax)*
    %Predict D_1^{k+1}
    $D_1^{k+1} := \chi_{D_1}(x, IOP, U, D_2^k, k_1^k, k_2^k);$
        %Predict D_2^{k+1}
        $\hookrightarrow D_2^{k+1} := \chi_{D_2}(x, IOP, U, D_1^{k+1} \ k_1^k \ k_2^k);$
            %Predict k_1^{k+1}
            $\hookrightarrow k_1^{k+1} := \chi_{k_1}(x, IOP, U, D_1^{k+1}, D_2^{k+1}, k_2^k);$
                %Predict k_2^{k+1}
                $\hookrightarrow k_2^{k+1} := \chi_{k_2}(x, IOP, U, D_1^{k+1}, D_2^{k+1}, k_1^{k+1});$
    %Check Cost Function
    $mat^{k+1} = (D_1^{k+1}, D_2^{k+1}, k_1^{k+1}, k_2^{k+1});$
    $error = \sum |mat^{k+1} - mat^k|;$
    %Update Next Iteration
    k=k+1;
END

2.6.2. Neighborhood-Based Protocol (K-nn Search)

Due to the coupled effects that geometry, IOP, and material properties have on the corneal

response (i.e., displacement), different combinations of parameters could exist that provide the

same maximum displacement (i.e., less rigid corneas subjected to a large IOP could experience

the same displacement to the air puff as a more rigid cornea subjected to a lower IOP), causing

the response surface approach to be less effective, i.e., Algorithm 1 could identify different sets

of material parameters according to the initial seed (local minima). The K–nn search approach

searches the set of material parameters directly in the raw dataset without the need for an approx-

imation function. This algorithm searches the *n* closest neighbors to the patient in the dataset and

then interpolates the material model parameters in terms of the distance from the patient's point

to the neighbors. The distance is calculated as the Euclidean distance in the (x, IOP, U) subspace

of the dataset.

13

2.7. Validation

To validate the proposed methodology, 5 eyes (1 healthy eye and 4 keratoconus eyes) that were subjected to a non-contact tonometry test (CorVis ST, Oculus, Germany) were considered. For these eyes, the corneal topography, IOP and corneal displacement due to the air puff, U, were available (see Table 1). These parameters were used to predict the patient's material model parameters using the previously described predictors. With the predicted material model parameters and the topographical data of the cornea, an *in silico* non-contact tonometry test was simulated using the procedure proposed in [4]. The numerical corneal displacement, U_{num}, was compared to the clinical displacement U.

Table 1: **Clinical Validation Data: CorVis Non-Contact Tonometry Test for Validation Patients (5 eyes: 1 healthy eye and 4 keratoconus eyes).**

L.	Eye	IOP	CCT	U	AL1	AL2	VA1	VA2	P. Dist.	R
h_0	R	12	578	1.00	2.09	1.92	0.19	-0.36	2.38	7.5
ktc_0	R	15	545	1.12	1.81	1.87	0.16	-0.34	5.07	7.58
ktc_1	L	15	544	1.03	1.84	2.06	0.18	-0.38	5.08	7.9
ktc_2	R	15	464	1.05	1.87	1.07	0.16	-0.43	2.53	7.6
ktc_3	L	16	460	1.12	1.84	2.06	0.17	-0.39	5.45	7.81

Table Legend and Units. **L.**: identification tag (i.e., 'h' for healthy eyes and 'ktc' for keratoconus eyes); **Eye**: ocular position; **IOP** [mmHg]: intraocular pressure; **CCT** [μm]: central corneal thickness; **U** [mm]: maximum deformation amplitude at the maximum concavity time; **AL1** [mm]: first applanation length; **AL2** [mm]: second applanation length; **VA1** [mm/s]: velocity at the first applanation time; **VA2** [mm/s]: velocity at the second applanation time; **P. Dist.** [mm]: peak distance; **R** [mm]: curvature at the maximum concavity time.

2.8. Computations and Statistical Analysis

Finite element simulations were conducted using the commercial finite element software Abaqus 6.11 (Dassault Systèmes Simulia Corp.). All the mathematical computations, algorithms and statistical analysis were developed using MATLAB R2012 v.8.0. software and open source C++ libraries (libSVM C++, [43]).

Data are reported as their mean and standard deviation (mean ± SD). Statistical significance was tested with the two-sample Kolmogorov-Smirnov test, where a two-sided p-value of less than 0.05 indicates significance. The performance of the predictors was measured in terms of the

14

coefficient of correlation R^2 to measure the quality of the fitting, whereas the Akaike information criterion (AIC) [44] was used to directly compare the quality of each model relative to each other.

3. Results

3.1. Monte Carlo Simulation

The Monte Carlo simulation computed 9,360 combinations. Due to technical limitations regarding the number of licenses, computations were performed on two conventional PCs with an 8-core processor and 8 GB RAM, requiring 128 days of computations on double thread. However, the methodology is implemented for a suitable parallel and massive computation on a computational cluster. The failure rate was under 3% of the computations, resulting in an effective dataset of 9,216 cases.

Figure 2: **Results of the Monte Carlo simulation.** **(a)** Mechanical corneal response to both experiments: inflation and air puff. The physiological range for the inflation is limited by the inflation real curves reported in the literature [24, 38] (see in black dashed lines and triangles), whereas the physiological range of the air-puff behavior must lie within the 'searching objective frame' (i.e., the reported experimental displacement to CorVis [1]). As shown in the 'upper right area', a physiological inflation behavior could not represent a physiological air-puff mechanical response, and thus, aiming out of the searching frame (see yellow vs. red lines in the figure); **(b)** First Monte Carlo analysis for pre-screening the range of the material parameters within the physiological inflation range reported. From all the simulations, the extreme ones were chosen for constraining the search space of the second Monte Carlo analysis. The range of the material parameters is shown in the bottom of the panel; **(c)** Second Monte Carlo analysis for establishing the range of the corneal mechanical response to an air-puff test. All the mechanical responses (incremental displacement due to the incremental pressure) related to the material range variation are depicted in a lighter color in the figures. Darker zones belong to those combinations of material parameters that numerically behaved as physiological with respect to the maximum deformation amplitude reported in the CorVis diagnosis. **(c.1)** Results of the Monte Carlo simulation for those eyes classified as healthy in the clinic (i.e., those whose topography and IOP were diagnosed as healthy by an optometrist). Dark red curves belong to the simulations that cast a numerical displacement that is contained within the experimental range ($U_{Healthy}[mm] \in (0.8, 1.1)$); **(c.2)** Results of the Monte Carlo simulation for those eyes classified as keratoconic in the clinic. Dark blue curves belong to the simulations that cast a numerical displacement that is contained within the experimental range ($U_{KTC}[mm] \in (0.95, 1.25)$); **(c.3)** Results of the Monte Carlo simulation for those eyes that were subjected to a LASIK surgery in the clinic. Dark green curves belong to the simulations that cast a numerical displacement that is contained within the experimental range ($U_{LASIK}[mm] \in (0.9, 1.15)$).

The simulations show that the proposed material model is adequate to reproduce both the inflation and the bending response of the cornea when subjected to an air puff for different levels of the IOP (see Fig.2.a). In particular, the range of parameters used for the Monte Carlo simulation is able to accommodate the experimental response to corneal inflation tests reported in the literature (see Fig. 2.b). Note that traditional model development for corneal mechanics has mainly considered inflation tests to identify the model parameters. However, when the response

15

to an air puff is considered, we found that there are a number of combinations for which the inflation response is within the experimental range but the corneal displacement due to the air puff is not. An example of this situation is given by the red and blue lines in Fig. 2.a. In both cases, the response to the inflation test is identical, but the response to the air,puff is not physiological for the red line. Therefore, from the total number of samples in the Monte Carlo simulation, only those samples that reconcile the response to an inflation and to an air,puff test to be within the experimental ranges[1, 45, 5] were considered. After including this exclusion criterion, only 29% (1127 of 3855) of the healthy cases, 30.5% (1327 of 4344) of the KTC cases, and 21.5% (219 of 1017) of the LASIK cases were included in the training dataset. The bright areas in Fig.2.c(1–3) (healthy: red; KTC: blue; LASIK: green) show the response to the air puff for the admitted samples.

The empirical distribution of the material parameters related to the matrix (D_1 and D_2) did not follow a uniform distribution, whereas those related to the fibers (k_1 and k_2) were found to be uniformly distributed (see A.6 in Appendix A). A Kolmogorov-Smirnov test shows non-significant differences between the material parameters of the healthy-LASIK and the KTC-LASIK populations (see in Table 2). In contrast, significant differences were found for D_1 and D_2 between the healthy-KTC populations.

Table 2: **Kolmogorov-Smirnov Hypothesis Test between Populations Regarding the Material Parameters.**

	D_1		D_2		k_1		k_2	
Comparison	**h**	**p–value**	**h**	**p–value**	**h**	**p–value**	**h**	**p–value**
Healthy–KTC	1	<0.001	0	0.058	0	0.328	0	0.983
Healthy–LASIK	0	0.869	0	0.779	0	0.584	0	0.482
KTC–LASIK	0	0.098	0	0.161	0	0.681	0	0.725

Table Legend. **h**: indicates the result of the hypothesis test (i.e., h=1 rejects the null hypothesis that both populations come from the same continuous probability distribution); **p–value**: asymptotic p–value of the test (i.e., p–value < 0.05 means that the null hypothesis can be rejected at a 5% significance level).

When the cornea is under the action of the IOP (i.e., its physiological stress state), the cornea is under a pure traction membrane stress state where the full cornea works in tension (i.e., both extracellular matrix and both families of collagen fibers), and therefore, no bending effects exist.

16

However, during an air puff, the cornea experiences bending. Whereas the anterior surface goes

from a traction state of stress to a compression state of stress, the posterior surface works in

tension. Hence, in the anterior corneal stroma, the collagen fibers are not contributing to load

bearing since they do not support buckling and the stiffness of the cornea mainly relies on the

extracellular matrix. At the same time, the collagen fibers on the posterior stroma suffer from

a higher elongation, resulting in an overall non-physiological state of stress. In this regard, due

to the action of the IOP, no significant differences in the maximum principal stress and in the

maximum principal stretch were observed between the different populations for both the ante-

rior and posterior corneal surfaces. In contrast, when the maximum principal stress and stretch

are compared at the instant of maximum corneal displacement, significant statistical differences

between all populations were found at the posterior surface (see Table 3). However, at the ante-

rior surface, significant differences were found only for the maximum principal stretch, whereas

for the maximum principal stress, differences were found only between the healthy and KTC

populations (see Table 3).

Table 3: **Kolmogorov-Smirnov Hypothesis Test between Populations Regarding the Stress-Strain Apical Behavior.**

| | **Anterior** | | | | **Posterior** | | | |
| | **Stretch** | | **Stress** | | **Stretch** | | **Stress** | |
Comparison	**h**	**p–value**	**h**	**p–value**	**h**	**p–value**	**h**	**p–value**
Healthy–KTC	1	<0.001	1	<0.001	1	<0.001	1	<0.001
Healthy–LASIK	1	<0.001	0	0.073	1	<0.001	1	<0.001
KTC–LASIK	1	<0.001	0	0.083	1	<0.001	1	0.049

Table Legend. **h**: indicates the result of the hypothesis test (i.e., h=1 rejects the null hypothesis that both populations come from the same continuous probability distribution); **p–value**: asymptotic p–value of the test (i.e., p–value < 0.05 means that the null hypothesis can be rejected at a 5% significance level).

3.2. Sensitivity Analysis

The sensitivity analysis and ANOVA conducted on the dataset (with the admitted samples

only) demonstrate the predominant role of the material parameters on U_{num} (see Fig.3.a). For

the entire population, ANOVA revealed that the most influential parameters are the material

parameters (D_1 and D_2), followed by the IOP and the central corneal thickness (CCT). When the

17

populations are considered separately (Fig.3.b and Fig.3.c, respectively), the general trends are kept for the healthy and LASIK populations. However, for the KTC population, the IOP appears to play a more important role than the material itself. In addition, the superior-inferior curvature slightly influences the numerical response for the KTC population. The results demonstrate the significant importance of the IOP on U for those cases in which the corneal thickness is lower relative to the healthy case (i.e., KTC and LASIK).

Figure 3: **Pareto chart representing the variables responsible for 95% of the mechanical response (displacement).** **(a)** Impact of the main variables on the mechanical response taking the entire dataset into account; **(b)** Impact of the main variables on the mechanical response taking the healthy cases of the dataset into account; **(c)** Impact of the main variables on the mechanical response taking the KTC cases of the dataset into account; **(d)** Impact of the main variables on the mechanical response taking the LASIK cases of the dataset into account. *Legend:* intraocular pressure (IOP), central corneal thickness (CCT), superior-inferior curvature of the eye (R_v), material parameters (D_1, D_2 and k_2) and interaction between material parameter D_1 and the intraocular pressure ($D_1 : IOP$).

In general, the sensitivity analysis showed that the most influential parameters on the displacement response (U_{num}) were the material parameters (D_1, D_2 and k_2), the intraocular pressure (IOP), and the central corneal thickness (CCT) in all populations. An exception is found for the superior-inferior curvature (R_V) for the KTC population. However, the most remarkable result is the negligible impact of the material parameter k_1 on the numerical response. Although k_1 cannot be removed from the simulations since it is a material parameter of the strain energy function (1), the result from the sensitivity analysis suggests that setting its value to its average (i.e., $k_1 = 19$ [kPa]) appears to be a reasonable choice in terms of developing the material predictors. Henceforth, the parameter k_1 is treated as a constant value, thereby avoiding the need to adjust or train a specific model for it, with a consequent reduction in computational cost.

3.3. Response surface predictor models (MLP, SVR and QRS)

According to the results from the sensitivity analysis, the predictive models were constructed considering D_1, D_2, k_2, IOP, CCT, and U_{num}, following the methodology described in *Materials and Methods*. Table 4 presents the main results from the fitting for the three models under consideration.

All response surface methods performed similarly, although the MLP model showed a slightly better performance (see the R^2 value in Table 4). All models (D_1, D_2, and k_2) presented a good

18

Table 4: **Accuracy for the four predictors (MLP: multiple layer perceptron; SVR: support vector regressor; SR: surface response) for the different populations (healthy, KTC and LASIK)**

	D_1								
	Healthy			**KTC**			**LASIK**		
Var	**MLP**	**SVR**	**QRS**	**MLP**	**SVR**	**QRS**	**MLP**	**SVR**	**QRS**
R^2	0.967	0.958	0.952	0.886	0.869	0.843	0.954	0.948	0.949
AIC	-1769	-1661	-1671	-1386	-1324	-1241	-404	-391	-396
μ_{res}	-0.002	-0.005	-0.002	0.000	0.002	0.001	-0.003	-0.003	0.000
σ_{res}	0.028	0.032	0.032	0.054	0.058	0.063	0.028	0.030	0.030

	D_2								
	Healthy			**KTC**			**LASIK**		
Var	**MLP**	**SVR**	**QRS**	**MLP**	**SVR**	**QRS**	**MLP**	**SVR**	**QRS**
R^2	0.962	0.954	0.952	0.905	0.897	0.864	0.963	0.968	0.956
AIC	2589	2663	2626	3302	3339	3467	600	584	613
μ_{res}	-0.295	-0.622	-0.312	0.165	0.193	-0.083	0.312	0.171	0.498
σ_{res}	5.408	5.912	5.653	8.273	8.606	9.874	5.043	4.656	5.413

	k_2								
	Healthy			**KTC**			**LASIK**		
Var	**MLP**	**SVR**	**QRS**	**MLP**	**SVR**	**QRS**	**MLP**	**SVR**	**QRS**
R^2	0.857	0.822	0.781	0.563	0.518	0.432	0.817	0.806	0.774
AIC	5337	5421	5464	6360	6411	6477	1289	1295	1308
μ_{res}	-10.970	-23.592	-18.253	-3.106	-8.900	-10.458	-7.413	-13.408	-10.401
σ_{res}	148.2	164.0	172.6	220.1	232.4	249.4	176.1	181.4	194.5

Table Legend. R^2: coefficient of determination; **AIC**: Akaike information criterion for the final adjusted model; μ_{res}: average of the residuals of the predicted response with respect to the expected response; σ_{res}: standard deviation of the residuals of the predicted response with respect to the expected response.

coefficient of determination (R^2) and a relatively low dispersion of the residuals (i.e., predicted response minus real response) with their mean around zero, with the exception of k_2, which presented a higher dispersion. This result was somewhat expected since D_1 and D_2 were the material parameters to which the corneal displacement was more sensitive. In general, the best fitting always corresponded to the healthy population, whereas the worst performance was always found for the LASIK population. These results could be thought to be related with the disruption of the collagen fibers due to the corneal flap generated during the surgery and its consequent loss of stiffness. However, since our models are phenomenological and not structural, the dispersion is hypothesized to be mainly associated with the abrupt change of the corneal curvature of the anterior surface due to the resulting flattened area induced by the surgery and the dispersion on the central corneal thickness. As mentioned in the *Materials and Methods* section, in addition to individual predictors of the material parameters for each of the populations, a predictor was fit for each material parameter but considering the entire dataset. No significant differences in

the results were obtained when compared with the predictors constructed for individual populations (results not shown). Therefore, in the following, only results corresponding to individual populations will be shown.

Regarding the Akaike information criterion, it remains almost constant between the methods (MLP, SVR and QSR) for the same parameter (D_1, D_2 and k_2), indicating that all models obtained similar quality on the adjustment. The residual analysis indicates that the best predictions (i.e., mean close to 0) always belong to the D_1 independently of the method and the population. In contrast, the worst predictions were always associated with k_2 independently of the method and the population. However, it is remarkable that the healthy population showed the best accuracy with respect to the rest of the populations, whereas the KTC population showed the worst accuracy. This finding could be explained by the inherent geometrical variability of the keratoconus. For this pathology, the location of the disease is not repeatable among patients, leading to a very heterogeneous distribution of geometrical features among patients. Conversely, the geometrical features of healthy eyes are more repeatable. Furthermore, the better accuracy of the D_1 and the D_2 parameters are directly supported by their importance on the corneal response of the model (see Fig.3).

3.4. Neighborhood-Based Protocol (K-nn Search)

The K-nn search method does not require the fitting of a particular mathematical function to predict the material parameters in terms of the corneal patient's geometric data and the mechanical response to the air puff since it simply searches for the closest point in the database to the patient's data (IOP, CCT and U). However, this method helps to demonstrate the inherent coupling that exists between CCT, IOP and U that has been demonstrated in previous studies [2].

Figure 4a shows that for a given value of the IOP, different combinations of the material properties and corneal thickness lead to the same corneal displacement, U (see red dots in Fig. 4a). Similarly, for a given corneal thickness, different combinations of material parameters and IOP provide the same corneal displacement as an air puff (see Fig.4.b). This result shows that different combinations of material parameters, IOP and CCT can lead to the same corneal displace-

20

Figure 4: **Coupled Effect of the Corneal Response (Patient h_0, Table 1).** All the healthy cases of the dataset are represented as blue dots in the figures. The biomarkers selected for determining the mechanical properties of the eye are shown to outline the coupling between different parameters: different combinations of thickness, material and intraocular pressure could lead to the same displacement. **(a)** Displacement (U) versus thickness (CCT) considering the intraocular pressure to be constant (IOP=12 mmHg). In red dots, all the feasible combinations of CCT that lead to the same displacement (1 mm) when the material properties and the pressure are fixed; **(b)** Displacement (U) versus IOP (IOP) considering the thickness to be constant (CCT=578 microns). In red dots, all the feasible combinations of IOP that lead to the same displacement (1 mm) when the material properties and the CCT are fixed; **(c)** Intraocular pressure (IOP) versus thickness (CCT) considering the displacement to be constant (U=1.00 mm). All tuples of IOP and CCT that can lead to the same displacement (1 mm). The dispersion of the parameters is only influenced by the tissue stiffness, i.e., the lowest pressures and thickness can only behave as the highest pressures and thickness if the material properties are stiffer. In this way, although different corneas could have a similar average tissue stiffness, an increase in IOP or CCT could lead to a less compliant mechanical response.

ment, U, thus making it impossible to quantify each contribution separately. However, when the patient-specific information (IOP, CCT, and U) is used as an input to the dataset (red triangle in Fig.4.c), it is possible to define a neighborhood of feasible points around the patient's data (blue diamonds in Fig.4.c) from which the material parameters can be estimated. This method is the most straightforward in terms of searching and implementation, as well as the one providing the best prediction (see next section). However, it is also the most expensive method in terms of computations since the accuracy of the method is highly affected by the resolution of the grid used for the dataset (number of samples present in the dataset).

3.5. Examples with clinical data

Table 5 shows the material model parameter predictions for the 5 patients described in Table 1. All the material model parameters obtained with the different predictors were used to simulate a non-contact tonometry test using the patient-specific data available for each case, i.e., topography of the cornea and IOP. For most cases, the predicted displacements (U_{num}) were in close proximity to the measured displacement (U), with the largest error difference, $\epsilon(\%)$, being 13% for the KTC eye (patient ktc2) and the QRS method. In addition, although local minima exist and we are aware of them, material predictions associated with local minima also lead to a predicted corneal displacement close to the actual measurements (results not shown). For patient ktc2, for which the material predictions led to the worst corneal displacement predictions, it was found that the closest neighbor to the patient's data was located at a distance that was an order of magnitude larger than for the other patients. This result indicates the need for a larger number

21

Table 5: **Validation using a priori unknown clinical patient data (Table 1). Application of the former patient-specific geometrical reconstruction algorithm [4] coupled with the present patient-specific material prediction methodology to reproduce the maximum deformation amplitude (displacement) of the corneal apex when subjected to a non-contact tonometry test (clinical values correspond to the CorVis measurement system).**

		Input	Output		Validation	
			D_1 | D_2 | k_1 | k_2		U_{num}	$\epsilon(\%)$
L.	Meth.		[kPa] | [–] | [kPa] | [–]		[mm]	[–]
h_0	K-nn	IOP=12 mmHg CCT=578 μm U=1.00 mm	0.277 | 120.6 | 20.8 | 516.9		1.007	0.726
	QRS		0.193 | 138.3 | 19.0 | 545.6		1.013	1.251
	MLP		0.446 | 85.7 | 19.0 | 843.1		1.022	2.158
	SVR		0.292 | 122.8 | 19.0 | 191.5		1.006	0.573
ktc_0	K-nn	IOP=15 mmHg CCT=545 μm U=1.12 mm	0.267 | 103.5 | 17.9 | 525.3		1.153	2.968
	QRS		0.289 | 97.9 | 19.0 | 455.5		1.175	4.917
	MLP		0.379 | 80.6 | 19.0 | 644.6		1.174	4.814
	SVR		0.368 | 81.3 | 19.0 | 687.4		1.171	4.503
ktc_1	K-nn	IOP=15 mmHg CCT=544 μm U=1.03 mm	0.330 | 109.0 | 17.6 | 374.5		1.025	0.529
	QRS		0.320 | 105.9 | 19.0 | 458.4		1.042	1.150
	MLP		0.186 | 131.3 | 19.0 | 443.0		1.072	4.099
	SVR		0.229 | 127.2 | 19.0 | 321.1		1.042	1.147
ktc_2	K-nn	IOP=15 mmHg CCT=464 μm U=1.05 mm	0.385 | 126.7 | 20.8 | 267.5		1.161	10.565
	QRS		0.363 | 122.0 | 19.0 | 540.0		1.186	12.964
	MLP		0.379 | 128.1 | 19.0 | 412.8		1.149	9.408
	SVR		0.365 | 126.1 | 19.0 | 423.3		1.175	11.857
ktc_3	K-nn	IOP=16 mmHg CCT=460 μm U=1.12 mm	0.388 | 120.5 | 18.5 | 592.7		1.131	0.940
	QRS		0.319 | 115.3 | 19.0 | 515.3		1.238	10.545
	MLP		0.336 | 122.1 | 19.0 | 397.0		1.198	6.933
	SVR		0.330 | 116.2 | 19.0 | 486.6		1.227	9.533

Table Legend. (D_1 [kPa] \| D_2 [–] \| k_1 [kPa] \| k_2 [–]): Parameters of the Demiray + G–H–O energy strain function ; U_{num} [mm]: maximum deformation amplitude provided by the numerical simulation of the non-contact tonometer; $\epsilon(\%) = |U_{num} - U|/U \cdot 100$: percentage difference between numerical and clinical displacement.

483 of samples in the dataset, i.e., a more dense sampling of the parameter space. However, note

484 that as the number of patients in the database increases, the prediction capabilities of all models

485 will also generally increase. Further information regarding the performance of each method can

486 be found in Appendix A. Regarding the time required to search a set of material parameters

487 (t_{exec}, Table A.6), the fastest method is the K–nn search since it does not require any iterative

488 procedure to find the material properties. In addition, depending on the initial material seed,

489 the iterative procedure may find different minima and take longer execution times. For these

490 reasons, the implementation of the algorithm includes a multiple seed strategy to identify the

22

491 material parameters with the least possible error.

4. Conclusions

493 A series of mathematical models have been proposed to predict the mechanical properties

494 of corneal tissue from patient-specific data obtained using a non-contact tonometry test. The

495 proposed methodology is based on *in silico* simulations of the non-contact tonometry tests using

496 patient-specific corneal geometry data [4]. The methodology is amenable for implementation

497 on commercial devices for clinical applications, and it provides acceptable execution times and

498 accuracy.

499 The computational simulation has different assumptions of the material and the modeling that

500 cannot be neglected. First, we used a phenomenological and macroscopic material model for

501 the cornea that allows to reproduce, within the experimentally reported range, the corneal re-

502 sponse to both inflation to increase values of IOP and the corneal displacement induced by a

503 non-contact tonometry test. Regarding the material model, there are some hypotheses that must

504 be addressed, such as the absence of viscoelasticity or the use of a generic orthogonal pattern

505 of fibers following that proposed by Meek et al. (2009) [50]. With respect to the viscoelastic

506 properties of the cornea, the loading of the tissue is fast enough to consider that viscoelastic

507 effects do not play a major role in the corneal response [46]. This assumption has been widely

508 accepted in previous publications (see several publications by Elsheikh, Pandolfi, Lanchares or

509 Studer), and recently, Simonini et al. (2016) [56] have reported a study on the dynamics of the

510 cornea when subjected to an air puff that suggests the great importance of the elastic contribution

511 of the stroma during the loading phase of the air jet but the minor contribution of the inertia

512 and viscoelasticity. However, if the recovery of the cornea during the unloading phase would

513 be addressed, the inclusion of inertia and viscoelasticity would be essential. Concerning the

514 pattern of collagen fibers is not patient specific since it is not yet easily accessible. Although

515 Winkler et al. and others authors have reported a more precise micro-structural distribution of

516 the fibers using SHG optical microscopy [51, 52, 53, 47, 48, 49], the inclusion of the patient-

517 specific micro-structural information of the cornea would not be useful but would rather increase

23

the computational costs and introduce a new bias since this information was not accessible for our patients. Nevertheless, the proposed methodology does not prevent the use of more complex material models that incorporate information of the micro-structure of the cornea, viscoelasticity or inertia. Second, the boundary condition simulating the air-jet impact has been assumed to be a constant pressure applied over the cornea. Although a CFD analysis has been applied over a generic cornea to compute the pressure pattern, a more precise simulation would require a fluid structure simulation since the corneal geometry and the deformation of the cornea over time may have an important impact on the pressure transferred during the air puff.

Despite its considerable computational cost, the Monte Carlo simulation has proven to be a powerful tool for use in real-time estimation of the corneal mechanical properties from a non-contact tonometry test in the clinic. In addition, the mathematical tools (MLP, SVR and QRS) have shown good performance in predicting the corneal material parameters, but the inherent coupling between the IOP, the CCT, and the corneal mechanical properties affecting the corneal response introduces an unavoidable dispersion in the data that reduces the performance of these methods. In this regard, the K–nn search has proven to be the most reliable method. Since it restricts the search to the neighborhood of the patient, the method is not prone to finding local minima, and it exhibits the best performance in terms of execution time. Furthermore, the material model parameters predicted by the K-nn search method lead to the most accurate predictions of the corneal displacement with respect to the clinical value (i.e., less than 3% difference with respect to the clinical results). Although the main drawback is the considerable computational cost involved in generating the dataset because it needs a fine resolution on the data grid for good accuracy, it is still more suitable than other optimization methods, such as the IFEM, due to its real-time response (i.e., no finite element computation is required for the diagnosis, but the patient can subsequently be used for updating the dataset).

No significant differences have been found between populations, in general, in terms of the material parameters. In this regard, only the healthy and KTC populations showed significant differences in terms of the D_1 and D_2 parameters but not in terms of k_1 and k_2. Therefore, these results indicate that considering differences in the material parameters of the cornea may not

24

be sufficient to classify healthy and keratoconus eyes using a single air-puff test, pointing to the necessity of having more than a single test for properly characterizing the properties of the eye. However, until now, there has been no additional in vivo test that complements the air-puff diagnosis, and the results should be assessed additionally by, for example, ex vivo inflation tests, as we used for constraining the search of material properties with both physiological behaviors (i.e., inflation and air puff). Moreover, our results suggest that variations in corneal thickness may be a more reliable monitoring variable in terms of classifying the healthy population from the KTC population. In addition, based on the finite element simulations, the maximum principal stretch in the anterior and posterior surfaces of the cornea obtained at the instant of maximum corneal deformation may be used as a discriminant to classify different groups (healthy, KTC and LASIK).

One final limitation regarding the clinical biomarkers used for the prediction must be addressed. For simplicity, only 3 clinical biomarkers have been used for predicting the material properties of the cornea: pressure (i.e., the IOP), geometry (i.e., CCT) and displacement (i.e., the maximum deformation amplitude of the CorVis test). Since our models are mainly phenomenological, macroscopic and are not taking the inertia, viscoelasticity and micro-structural features of the cornea into account, the dynamic parameters provided by the CorVis diagnosis test cannot be trustworthily used. Moreover, ANOVA and the Pareto analysis showed that for the models used in the present study, the most influential parameters were the selected ones. However, there are no problems for easily introducing other corneal parameters in the predictive model, provided that they can be accurately measured in both the experimental and the numerical results. Although only these 3 biomarkers have been used, the methodology has been tested with actual unknown patient data that did not form a part of the dataset. The predicted material parameters, along with the patient's corneal geometry and IOP, were used to simulate a non-contact tonometry test to predict the corneal displacement. The numerical results resulted in errors of less than 10% in most cases, with the K-nn search methodology outperforming the response surface-based methods, achieving errors of less than 3%.

The important aspect of the present study is that the proposed methodology, independently of

25

the complexity of the numerical simulations, is amenable for real-time diagnosis and implementation in commercial devices. Importantly, it allows easily introducing additional elements (e.g., viscoelasticity, microstructure, dynamics, and so forth) that could enhance the performance and accuracy of the results without modifying the underlying methodology. Eventually, the computational framework will incorporate actual clinical data (corneal topographies, IOP and corneal apical displacement from a non-contact tonometry test) to predict the mechanical properties of the cornea. These results could be used for surgical planning or to monitor the evolution of a given patient by looking at changes in the mechanical properties with time.

Appendix A. Additional Results

This appendix contains the extended non-essential results that are needed to understand the complete scope of the outcomes. The extensions are related to the following:

- **Sensitivity analysis**: The response surface ($U = f(geometry, pressure, material)$) used for analyzing the impact of the different variables (geometry, pressure and material) to the numerical variable under analysis in the FE computation (displacement) is depicted in Fig.A.5.

- **Statistical distribution of the mechanical properties of the cornea for the Monte Carlo simulation**: All the Monte Carlo combinations of material that fulfill both physiological responses (inflation and air puff) are presented in Fig.A.6 (green histogram). Whereas the parameters related to the fibers are uniformly distributed (k_1 and k_2), the matrix parameters (D_1 and D_2) stack around 0.4–0.45 [kPa] and [130–140].

- **Accuracy of the prediction after the training phase for the SVR and MLP**: The accuracy of the predictions of both methods after the training phase is depicted in Fig.A.7. Support vector regressor does not present a blue shaded zone since only one SVR is used. Conversely, the MLP uses 7 different assemblies and subsequently computes the average. Therefore, the confidence intervals (blue shaded zones) can be established.

- **Goodness of the fits for the SVR, MLP and QRS models**: The correlation plot of the predicted property versus the actual value in the dataset is depicted in Fig.A.8. The material properties D_1 and D_2 show the best model fitting, whereas k_2 shows a higher dispersion (k_1 is not shown since it was discarded after the sensitivity analysis).

- **Additional performance of the methodology**: The results of supplementary performance variables (execution time, distance of the nearest neighbor and initial tangent modulus) are depicted in Table A.6.

Figure A.5: **Slice plots of the quadratic response surface for each population (healthy–red, KTC–blue, LASIK–green).** The slice plots show the individual contribution of the different model parameters on the numerical displacement. The higher the slope, the higher the contribution (shaded zones represent the standard deviation of the parameter, whereas solid lines represent the mean response). **(a)** Impact of the model parameters on the numerical displacement of the healthy population; **(b)** Impact of the model parameters on the numerical displacement of the KTC population; **(c)** Impact of the model parameters on the numerical displacement of the LASIK population

Figure A.6: **Statistical distribution of the mechanical properties of the cornea for the Monte Carlo simulation.** The empirical distribution (green histogram) due to all the combinations of material parameters that fulfill both physiological behaviors (inflation and air puff) shows that the fiber's parameters are uniformly distributed.

Figure A.7: **MLP (right panel) and SVR (left panel) predictions for validating the training phase (only healthy response is shown).** **a.(1–3)**: D_1, D_2 and k_2 predictions depending on the patient case for the MLP method. Blue intervals correspond to the confidence interval (95% light blue and 99% dark blue) of the prediction since the method is composed of an ensemble of 7 independent MLPs and the response is the average of each independent MLP; **b.(1–3)**: D_1, D_2 and k_2 predictions depending on the patient case for the SVR method. k_1 predictor is not computed since it was discarded after the sensitivity analysis.

Figure A.8: **Correlation plot of the predicted parameter (y-axis) vs expected parameter (x-axis) for the healthy group. a.(1–3)**: QRS; **b.(1–3)**: MLP; **c.(1–3)**: SVR. D_1 and D_2 show a good prediction of the values, whereas k_2 presents a higher dispersion. k_1 predictor is not computed since it was discarded after the sensitivity analysis.

Table A.6: **Performance of the Prediction of the Patient-Specific Material Properties for the Clinical Patients (Table 1) Applying the Prediction Models (K-nn Search: Neighbor-based Prediction Model; QRS: Quadratic Response Surface Model; MLP: Multiple Layer Perceptron; SVR: Support Vector Regressor)**

| L.	Meth.	t_{exec} [s]	Dist. [–]	E [kPa]	E (%) [–]
h_0	K-nn	0.060 ± 0.023	0.003	283.637	–
	QRS	1.996 ± 0.562	–	236.15	-16.7
	MLP	19.282 ± 9.551	–	305.333	7.7
	SVR	75.304 ± 4.469	–	291.146	2.7
ktc_0	K-nn	0.036 ± 0.002	0.006	237.407	–
	QRS	1.145 ± 0.101	–	245.760	3.5
	MLP	14.473 ± 1.458	–	259.284	9.2
	SVR	7.833 ± 4.724	–	255.510	7.6
ktc_1	K-nn	0.036 ± 0.003	0.005	286.22	–
	QRS	0.781 ± 0.028	–	279.328	-2.4
	MLP	17.861 ± 2.922	–	222.531	-22.3
	SVR	10.130 ± 2.168	–	250.773	-12.4
ktc_2	K-nn	0.0336 ± 0.003	0.025	375.877	–
	QRS	0.460 ± 0.015	–	341.716	-9.1
	MLP	4.962 ± 0.238	–	367.299	-2.3
	SVR	2.284 ± 0.187	–	352.159	-6.3
ktc_3	K-nn	0.035 ± 0.003	0.006	354.524	–
	QRS	0.519 ± 0.018	–	296.684	-16.3
	MLP	7.892 ± 0.160	–	322.154	-9.1
	SVR	4.091 ± 0.269	–	306.076	-13.7

Table Legend. t_{exec} [s]: execution time for prediction; **Dist. [–]**: minimum distance of the neighborhood (only for K-nn search); $E = 6 \cdot D_1 D_2 + 4 \cdot k_1$ [kPa]: Equivalent initial tangent modulus ($\lambda = 1$); $E(\%) = 100 \cdot (1 - E_j / E_{K-nn})$: initial slope difference between the equivalent initial tangent modulus of the 'j' method (E_j), where 'j' are QRS, MLP, and SVR, with respect to the equivalent initial tangent modulus of the K-nn search method (E_{K-nn}).

[1] M. Lanza, S. Iaccarino, M. Bifani, In vivo human corneal deformation analysis with a scheimpflug camera, a critical review., J. Biophotonics 9(5) (2016) 464–477.

[2] M. Á. Ariza-Gracia, J. F. Zurita, D. P. Piñero, J. F. Rodriguez-Matas, B. Calvo, Coupled biomechanical response of the cornea assessed by non-contact tonometry. a simulation study, PLoS One 10 (3) (2015) e0121486.

[3] A. Sinha Roy, M. Kurian, H. Matalia, R. Shetty, Air-puff associated quantification of non-linear biomechanical properties of the human cornea in vivo, J. Mech. Behav. Biomed. Mater. 48 (2015) 173–182.

[4] M. Á. Ariza-Gracia, J. Zurita, D. P. Piñero, B. Calvo, J. F. Rodríguez-Matas, Automatized patient-specific methodology for numerical determination of biomechanical corneal response, Ann. Biomed. Eng. 44(5) (2016) 1753–1772.

[5] Z. Hassan, L. Modis, Jr, E. Szalai, A. Berta, G. Nemeth, Examination of ocular biomechanics with a new scheimpflug technology after corneal refractive surgery, Cont. Lens Anter. Eye 37(5) (2014) 337–341.

[6] F. Faria-Correia, I. Ramos, B. Valbon, A. Luz, C. J. Roberts, R. Ambrósio, Jr, Scheimpflug-based tomography and biomechanical assessment in pressure-induced stromal keratopathy, J. Refract. Surg. 29 (5) (2013) 356–358.

[7] Y. Hon, A. K. C. Lam, Corneal deformation measurement using scheimpflug noncontact tonometry, Optom. Vis. Sci. 90 (1) (2013) e1–e8.

[8] J. Hong, J. Xu, A. Wei, S. X. Deng, X. Cui, X. Yu, X. Sun, A new tonometer–the corvis st tonometer: clinical comparison with noncontact and goldmann applanation tonometers, Invest. Ophthalmol. Vis. Sci. 54 (1) (2013) 659–665.

[9] S. Kling, S. Marcos, Contributing factors to corneal deformation in air puff measurements, Invest. Ophthalmol. Vis. Sci. 54 (7) (2013) 5078–5085.

[10] C. J. Roberts, Concepts and misconceptions in corneal biomechanics, J. Cataract Refract. Surg. 40 (6) (2014) 862–869.

[11] P. M. Pinsky, D. V. Datye, A microstructurally-based finite element model of the incised human cornea, J. Biomech. 24 (10) (1991) 907–922.

[12] P. M. Pinsky, D. van der Heide, D. Chernyak, Computational modeling of mechanical anisotropy in the cornea and sclera, J. Cataract Refract. Surg. 31 (1) (2005) 136–145.

[13] M. Lago, M. Rupérez, F. Martínez-Martínez, C. Monserrat, E. Larra, J. Güell, C. Peris-Martínez, A new methodology for the in vivo estimation of the elastic constants that characterize the patient-specific biomechanical behavior of the human cornea, J. Biomech. 48 (1) (2015) 38–43.

[14] A. Pandolfi, F. Manganiello, A model for the human cornea: constitutive formulation and numerical analysis, Biomech. Model. Mechanobiol. 5 (4) (2006) 237–246.

[15] A. Pandolfi, G. A. Holzapfel, Three-dimensional modeling and computational analysis of the human cornea considering distributed collagen fibril orientations, J. Biomech. Eng. 130 (6) (2008) 061006.

[16] E. Lanchares, B. Calvo, J. A. Cristóbal, M. Doblaré, Finite element simulation of arcuates for astigmatism correction, J. Biomech. 41 (4) (2008) 797–805

[17] H. P. Studer, H. Riedwyl, C. A. Amstutz, J. V. M. Hanson, P. Büchler, Patient-specific finite-element simulation of

652 the human cornea: a clinical validation study on cataract surgery, J. Biomech. 46 (4) (2013) 751–758.

653 [18] F. Bao, M. Deng, Q. Wang, J. Huang, J. Yang, C. Whitford, B. Geraghty, A. Yu, A. Elsheikh,Evaluation of the

654 relationship of corneal biomechanical metrics with physical intraocular pressure and central corneal thickness in

655 ex vivo rabbit eye globes, Exp. Eye Res. 137 (2015) 11–17.

656 [19] Kok, Schalk and Botha, Natasha and Inglis, Helen M, Calibrating corneal material model parameters using only

657 inflation data: An ill-posed problem, International Journal of Numerical Methods in Biomedical Engineering, 30:12

658 (2014) 1460–1475

659 [20] Girard, Michaël J A. and Downs, J Crawford and Bottlang, Michael and Burgoyne, Claude F. and Suh, J-K Francis.,

660 Peripapillary and posterior scleral mechanics–part II: experimental and inverse finite element characterization., J

661 Biomech Eng, 131:5 (2009) DOI: 10.1115/1.3113683

662 [21] Girard, Michaël J A. and Downs, J Crawford and Burgoyne, Claude F. and Suh, J-K Francis., Peripapillary and

663 posterior scleral mechanics–part I: development of an anisotropic hyperelastic constitutive model., J Biomech Eng,

664 131:5 (2009), DOI: 10.1115/1.3113682

665 [22] Nguyen, T. D. and Boyce, B. L., An inverse finite element method for determining the anisotropic properties of the

666 cornea., Biomech Model Mechanobiol, 10:3 (2011) 323–337 DOI: 10.1007/s10237-010-0237-3

667 [23] A. Elsheikh, A. Joda, A. Abass, D. Garway-Heath, Assessment of the ocular response analyzer as an instrument

668 for measurement of intraocular pressure and corneal biomechanics, Curr. Eye Res. 40 (11) (2015) 1111–1119.

669 [24] C. Whitford, H. Studer, C. Boote, K. M. Meek, A. Elsheikh, Biomechanical model of the human cornea: consid-

670 ering shear stiffness and regional variation of collagen anisotropy and density, J. Mech. Behav. Biomed. Mater. 42

671 (2015) 76–87.

672 [25] E. Lanchares, M. A. del Buey, J. A. Cristóbal, L. Lavilla, B. Calvo, Biomechanical property analysis after corneal

673 collagen cross-linking in relation to ultraviolet a irradiation time, Graefes Arch. Clin. Exp. Ophthalmol 249 (8)

674 (2011) 1223–1227.

675 [26] R. Navarro, F. Palos, E. Lanchares, B. Calvo, J. A. Cristóbal, Lower- and higher-order aberrations predicted by an

676 optomechanical model of arcuate keratotomy for astigmatism, J. Cataract Refract. Surg. 35 (1) (2009) 158–165.

677 [27] A. S. Roy, W. J. Dupps, Jr, Patient-specific modeling of corneal refractive surgery outcomes and inverse estimation

678 of elastic property changes, J. Biomech. Eng. 133 (1) (2011) 011002.

679 [28] S. Kling, N. Bekesi, C. Dorronsoro, D. Pascual, S. Marcos, Corneal viscoelastic properties from finite-element

680 analysis of in vivo air-puff deformation, PLoS One 9 (8) (2014) e104904.

681 [29] F. Boschetti, V. Triacca, L. Spinelli, A. Pandolfi, Mechanical characterization of porcine corneas, J. Biomech. Eng.

682 134(3) (2012) 031003.

683 [30] J.-D. Ho, C.-Y. Tsai, R. J.-F. Tsai, L.-L. Kuo, I.-L. Tsai, S.-W. Liou, Validity of the keratometric index: evaluation

684 by the pentacam rotating scheimpflug camera, J. Cataract. Refract. Surg. 34 (1) (2008) 137–145.

685 [31] D. Smadja, D. Touboul, A. Cohen, E. Doveh, M. R. Santhiago, G. R. Mello, R. R. Krueger, J. Colin, Detection

686 of subclinical keratoconus using an automated decision tree classification, Am. J. Ophthalmol. 156 (2) (2013)

687   237–246.e1.

[32] M. A. Valdés-Mas, J. D. Martín-Guerrero, M. J. Rupérez, F. Pastor, C. Dualde, C. Monserrat, C. Peris-Martínez,
      A new approach based on machine learning for predicting corneal curvature (k1) and astigmatism in patients with
      keratoconus after intracorneal ring implantation, Comput. Meth. Prog. Bio. 116 (1) (2014) 39–47.

[33] P. A. Accardo, S. Pensiero, Neural network-based system for early keratoconus detection from corneal topography,
      J. Biomed. Inform. 35 (3) (2002) 151–159.

[34] M. C. Arbelaez, F. Versaci, G. Vestri, P. Barboni, G. Savini, Use of a support vector machine for keratoconus and
      subclinical keratoconus detection by topographic and tomographic data, Ophthalmology 119 (11) (2012) 2231–
      2238.

[35] E. Soudah, J. F. Rodriguez, R. Lopez, Mechanical stress in abdominal aortic aneurysms using artificial neural
      networks, J. Mech. Med. Biol. 15 (03) (2015) 1550029.

[36] E. Businaro, H. Studer, B. Pajic, P. Büchler, Gaussian process prediction of the stress-free configuration of pre-
      deformed soft tissues: Application to the human cornea, Med. Eng. Phys. 38 (4) (2016) 339–345.

[37] J. Krenek, K. Kuca, A. Bartuskova, O. Krejcar, P. Maresova, V. Sobeslav, Artificial neural networks in biomedicine
      applications, in: Proceedings of the 4th International Conference on Computer Engineering and Networks,
      Springer, 2015, pp. 133–139.

[38] M. R. Bryant, P. J. McDonnell, Constitutive laws for biomechanical modeling of refractive surgery,
      J. Biomech. Eng. 118 (4) (1996) 473–481.

[39] Y. S. Rabinowitz, Keratoconus, Surv. Ophthalmol. 42 (4) (1998) 297–319.

[40] T. C. Gasser, R. W. Ogden, G. A. Holzapfel, Hyperelastic modeling of arterial layers with distributed collagen fiber
      orientations, J. R. Soc. Interface 3 (6) (2006) 15–35.

[41] A. Eilaghi, J. G. Flanagan, I. Tertinegg, C. A. Simmons, G. Wayne Brodland, C. R. Ethier, Biaxial mechanical
      testing of human sclera, J. Biomech. 43 (9) (2010) 1696–1701

[42] M. Á. Ariza-Gracia, D. P. Piñero, J. F. Rodriguez-Matas, R. J. Pérez-Cambrodí, B. Calvo, Interaction between
      diurnal variations of intraocular pressure, pachymetry, and corneal response to an air puff: Preliminary evidence,
      JCRS Online Case Reports 3 (2015) 12–15.

[43] C. C. Chang, C. J. Lin, Libsvm: a library for support vector machines, ACM T. Intel. Syst. Tech. 2 (3) (2011) 27.

[44] Y. Sakamoto, M. Ishiguro, G. Kitagawa, Akaike information criterion statistics, D. Reidel Publishing Company,
      1999.

[45] T. Huseynova, G. O. Waring, 4th, C. Roberts, R. R. Krueger, M. Tomita, Corneal biomechanics as a function of
      intraocular pressure and pachymetry by dynamic infrared signal and scheimpflug imaging analysis in normal eyes,
      Am. J. Ophthalmol. 157 (4) (2014) 885–893.

[46] J. Simo, On a fully three-dimensional finite-strain viscoelastic damage model: formulation and computational
      aspects, Comput. Methods Appl. Mech. Engrg. 60 (2) (1987) 153–173.

[47] Benoit, Aurélie and Latour, Gaël and Marie-Claire, Schanne-Klein and Allain, Jean-Marc. Simultaneous mi-

32

crostructural and mechanical characterization of human corneas at increasing pressure., J Mech Behav Biomed Mater, 60 (2016) 93–105 DOI: 10.1016/j.jmbbm.2015.12.031

[48] Gusachenko, Ivan and Tran, Viet and Goulam Houssen, Yannick and Allain, Jean-Marc and Schanne-Klein, Marie-Claire, Polarization-resolved second-harmonic generation in tendon upon mechanical stretching., Biophys J, 102:9 (2012) 2220–2229 DOI: 10.1016/j.bpj.2012.03.068

[49] Latour, Gaël and Gusachenko, Ivan and Kowalczuk, Laura and Lamarre, Isabelle and Schanne-Klein, Marie-Claire, In vivo structural imaging of the cornea by polarization-resolved second harmonic microscopy., Biomed Opt Express, 3:1 (2012) 1–15 DOI: 10.1364/BOE.3.000001

[50] Meek, Keith M. and Boote, Craig., The use of X-ray scattering techniques to quantify the orientation and distribution of collagen in the corneal stroma., Prog Retin Eye Res, 28:5 (2009) 369–392 DOI: 10.1016/j.preteyeres.2009.06.005

[51] Winkler, Moritz and Chai, Dongyul and Kriling, Shelsea and Nien, Chyong Jy and Brown, Donald J. and Jester, Bryan and Juhasz, Tibor and Jester, James V., Nonlinear optical macroscopic assessment of 3-D corneal collagen organization and axial biomechanics., Invest Ophthalmol Vis Sci, 52:12 (2011) 8818–8827 DOI: 10.1167/iovs.11-8070

[52] Winkler, Moritz and Shoa, Golroxan and Xie, Yilu and Petsche, Steven J. and Pinsky, Peter M. and Juhasz, Tibor and Brown, Donald J. and Jester, James V., Three-dimensional distribution of transverse collagen fibers in the anterior human corneal stroma., Invest Ophthalmol Vis Sci, 54:12 (2013) 7293–7301 DOI: 10.1167/iovs.13-13150

[53] Winkler, Moritz and Shoa, Golroxan and Tran, Stephanie T. and Xie, Yilu and Thomasy, Sarah and Raghunathan, Vijay K. and Murphy, Christopher and Brown, Donald J. and Jester, James V., A Comparative Study of Vertebrate Corneal Structure: The Evolution of a Refractive Lens., Invest Ophthalmol Vis Sci, 56:4 (2015) 2764–2772 DOI: 10.1167/iovs.15-16584

[54] Simonini I., Pandolfi A., Customized Finite Element Modelling of the Human Cornea., PLoS One, 10:6 (2015) DOI: 10.1371/journal.pone.0130426

[55] Simonini I., Pandolfi A., The influence of intraocular pressure and air jet pressure on corneal contactless tonometry tests., J Mech Behav Biomed Mater, 58 (2016) 75–89 DOI: 10.1016/j.jmbbm.2015.07.030

[56] Simonini I., Angelillo M., Pandolfi A., Theoretical and numerical analysis of the corneal air puff test, Journal of the Mechanics and Physics of Solids, 93 (2016) 118–134 DOI: 10.1016/j.jmps.2016.04.012

[57] Rosenblatt, F. Principles of Neurodynamics: Perceptrons and the Theory of Brain Mechanisms. Spartan Books, Washington DC, 1961

[58] Cortes C., Vapnik V., Support-vector Networks, Machine Learning, 20:3 (1995), 273–297, DOI: 10.1007/BF00994018

[59] Drucker H., Burges C. J. C., Kaufman L., Smola A. J., Alexander J., Vapnik V. N. Support Vector Regression Machines, Advances in Neural Information Processing Systems, 9 (1996), 155–161

[60] Douglas C. M., Design and Analysis of Experiments, John Wiley & Sons, 5ed (2001) ISBN 0-471-31649-0
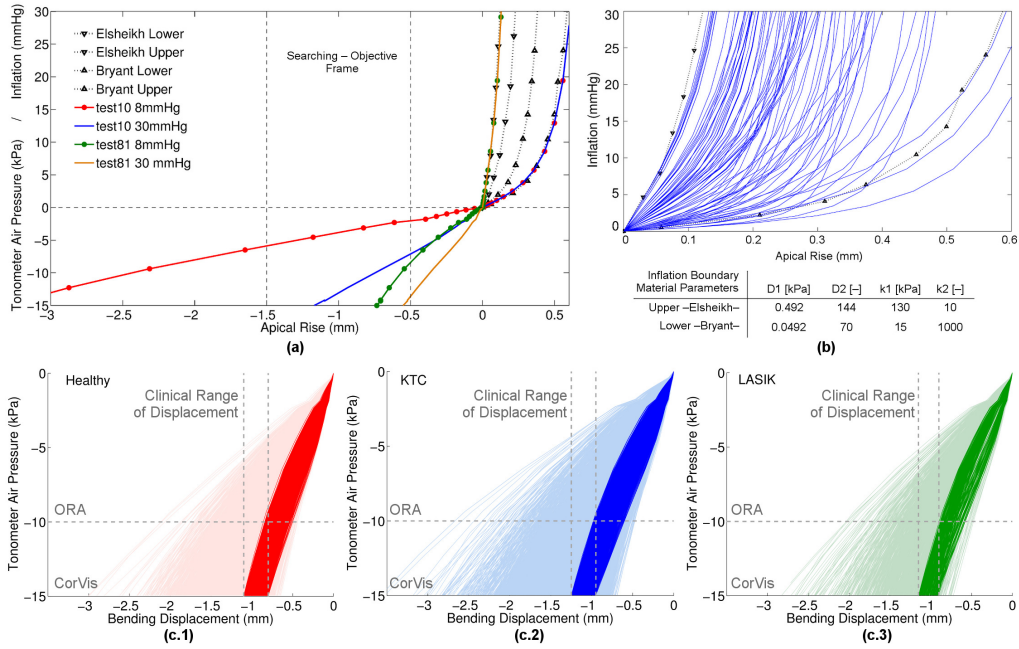
33

802 **Figures**
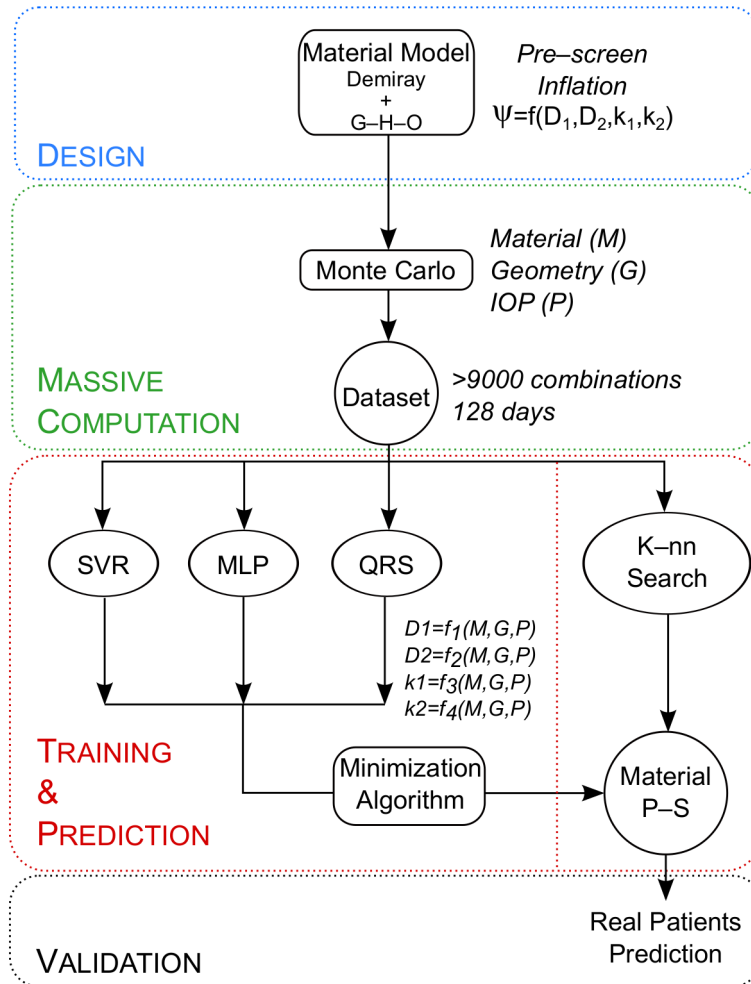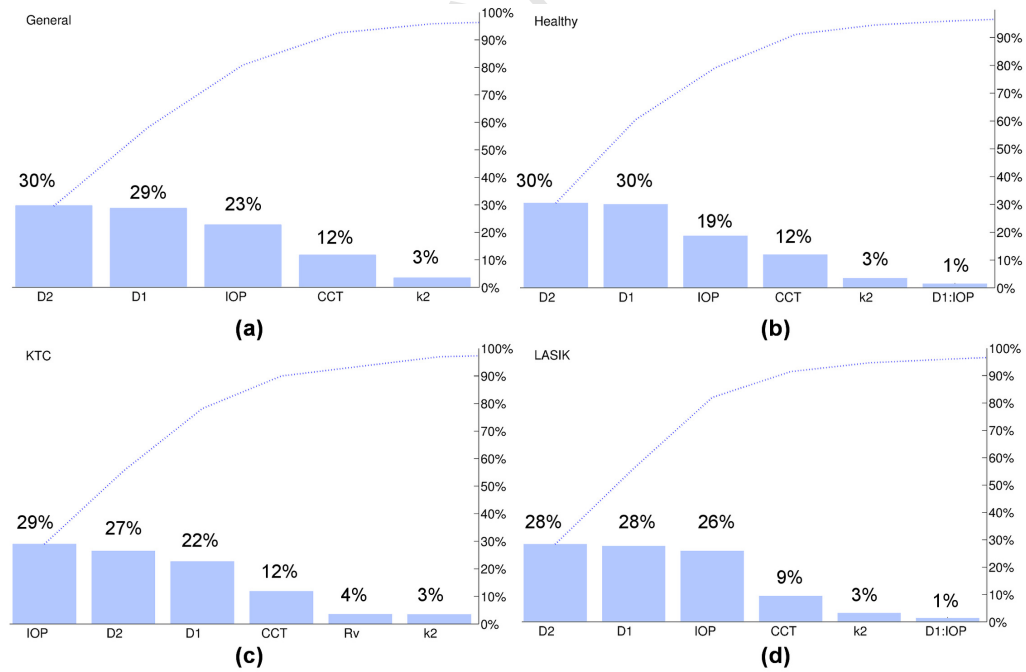

Figure A.9: **Figure 1**
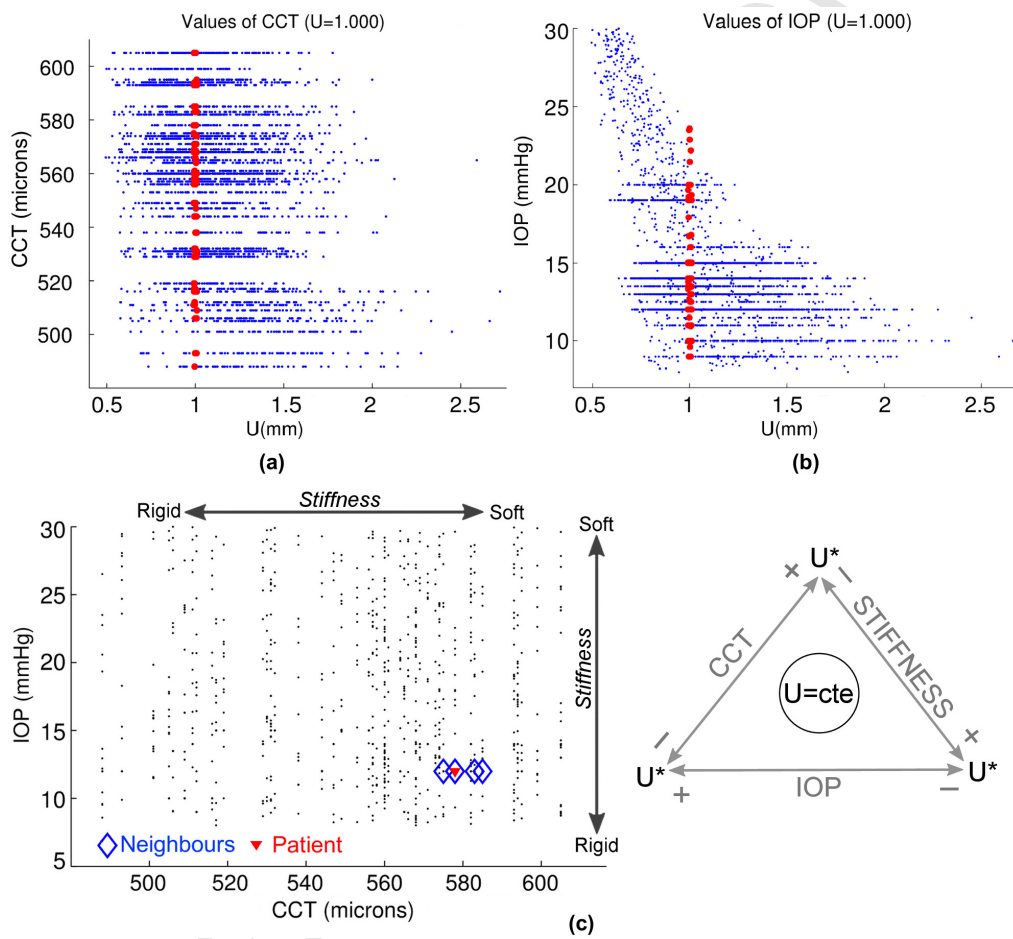
Figure A.10: **Figure 2**

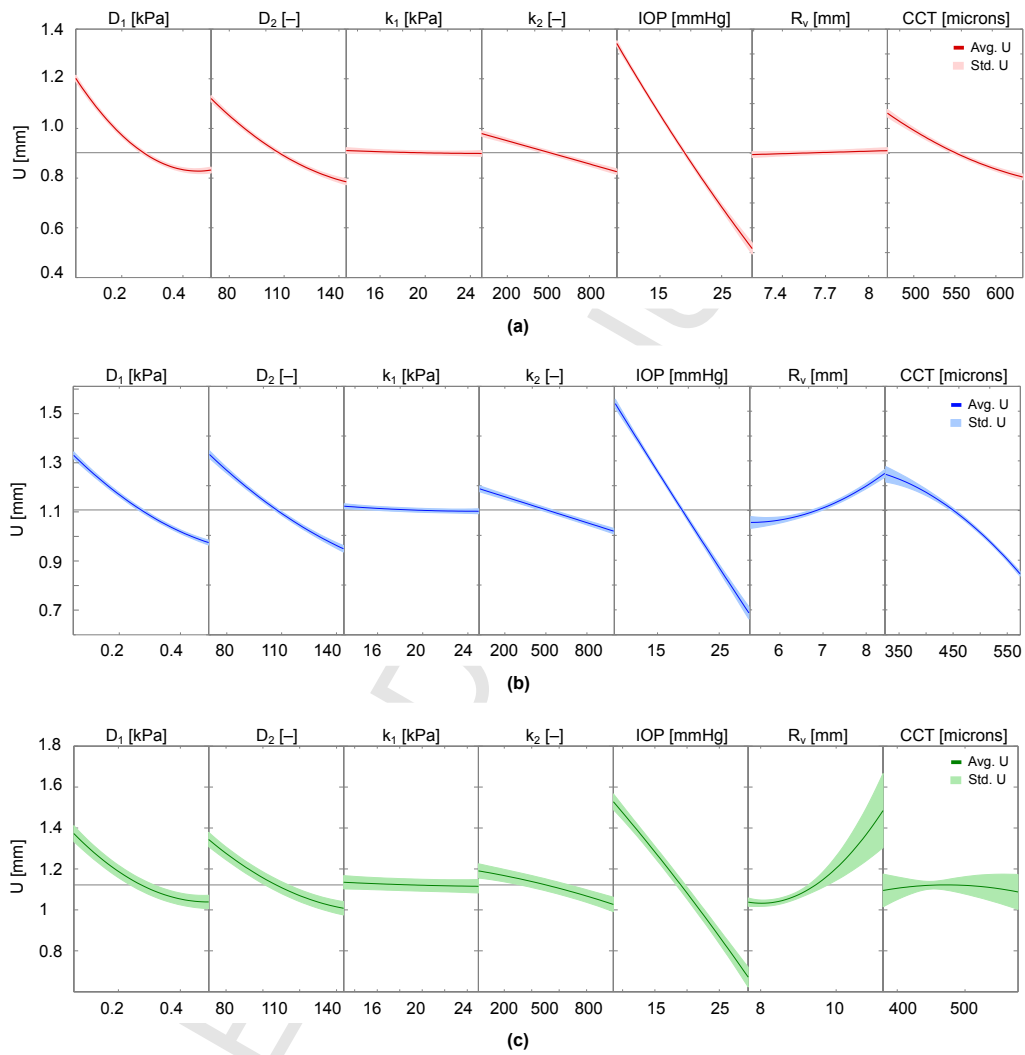
Figure A.11: **Figure 3**
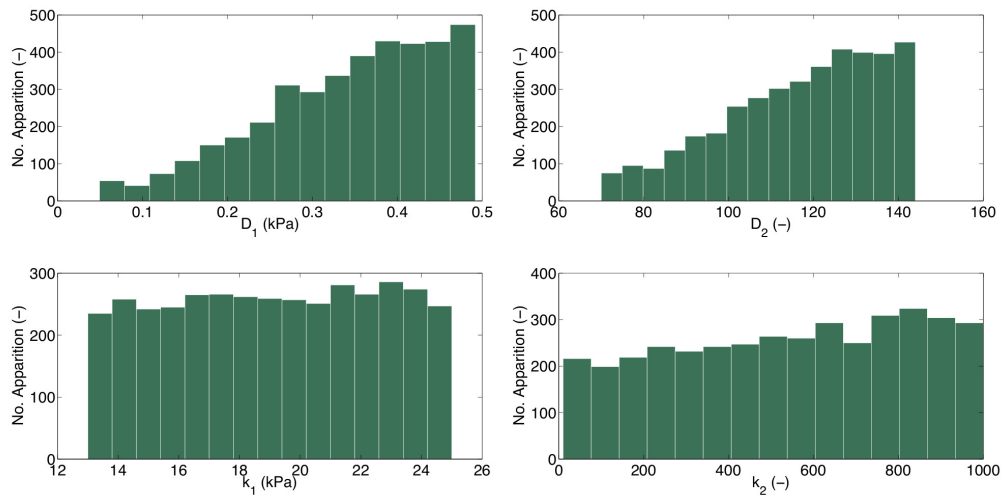
Figure A.12: **Figure 4**
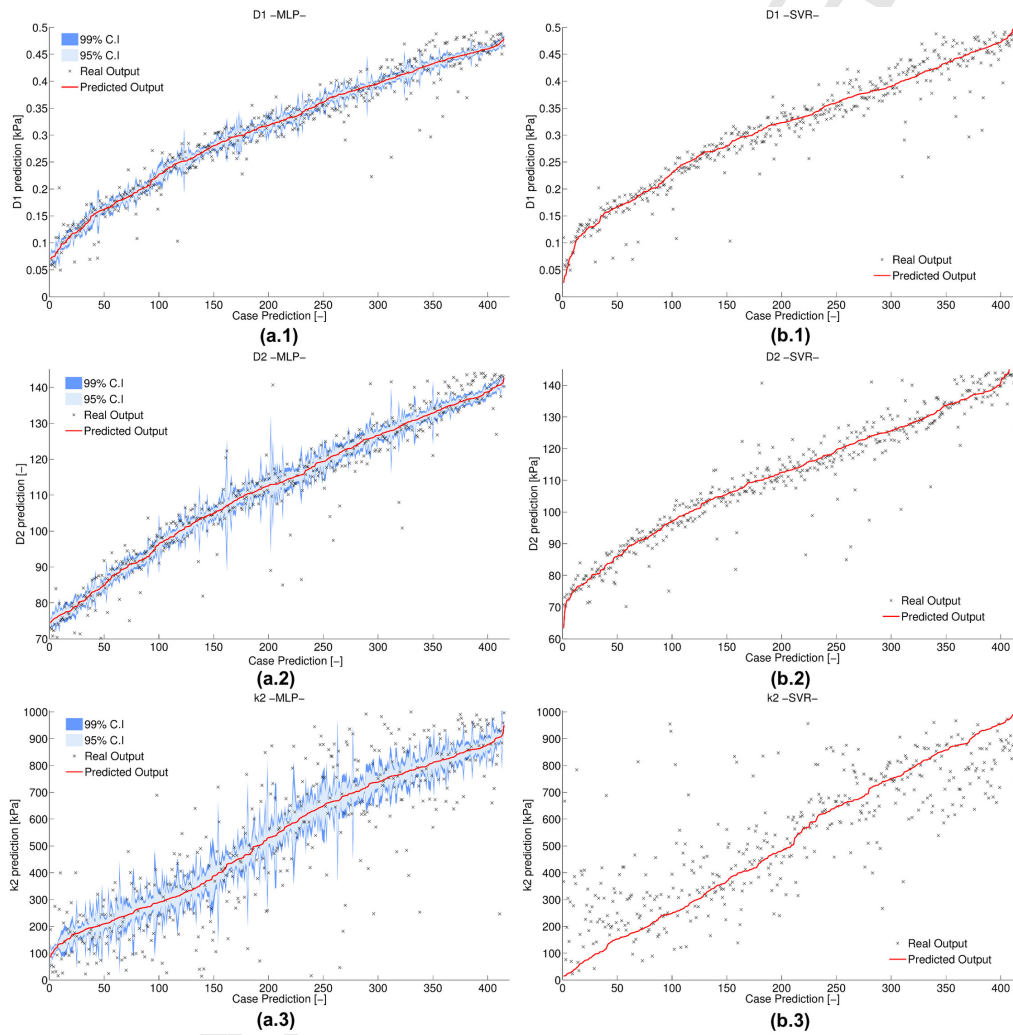
Figure A.13: **Figure A5**

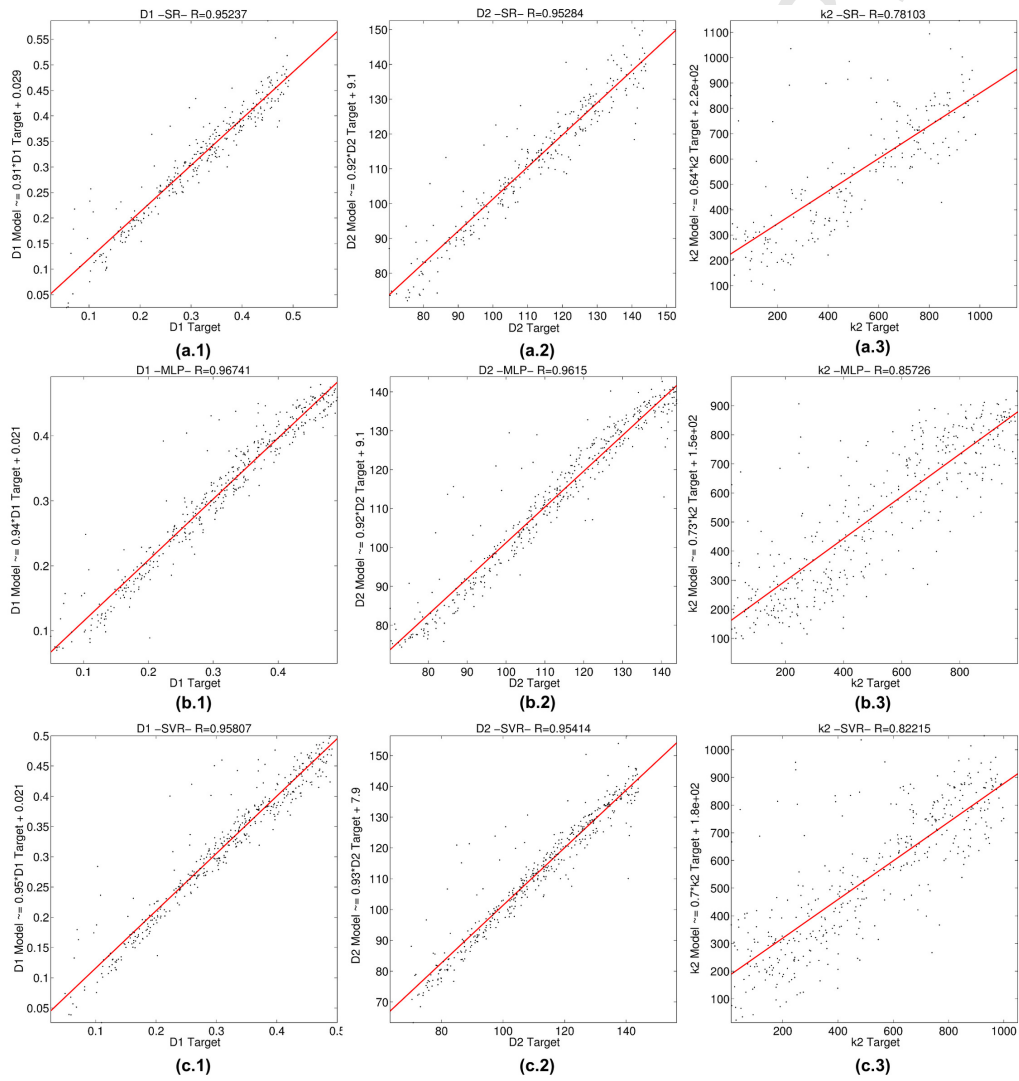Figure A.14: **Figure A6**

Figure A.15: **Figure A7**

Figure A.16: **Figure A8**